Molecular Structure of Canonical Liquid Crystal Interfaces

Monirosadat Sadati,[†,¶,#] Hadi Ramezani-Dakhel,[†,‡,¶] Wei Bu,[§] Emre Sevgen,[†] Zhu Liang,[∥] Cem Erol,[∥] Mohammad Rahimi,[†] Nader Taheri Qazvini,[#] Binhua Lin,[§] Nicholas L. Abbott,[⊥] Benoît Roux,*[,‡] Mark L. Schlossman,*[,∥] and Juan J. de Pablo*[,†,#]

[†]Institute for Molecular Engineering, [‡]Department of Biochemistry and Molecular Biology, and [§]Center for Advanced Radiation Sources, University of Chicago, Chicago, Illinois 60637, United States

[∥]Department of Physics, University of Illinois at Chicago, Chicago, Illinois 60607, United States

[⊥]Department of Chemical and Biological Engineering, University of Wisconsin−Madison, Madison, Wisconsin 53706, United States

[#]Argonne National Laboratory, Argonne, Illinois 60439, United States

Ⓢ *Supporting Information*
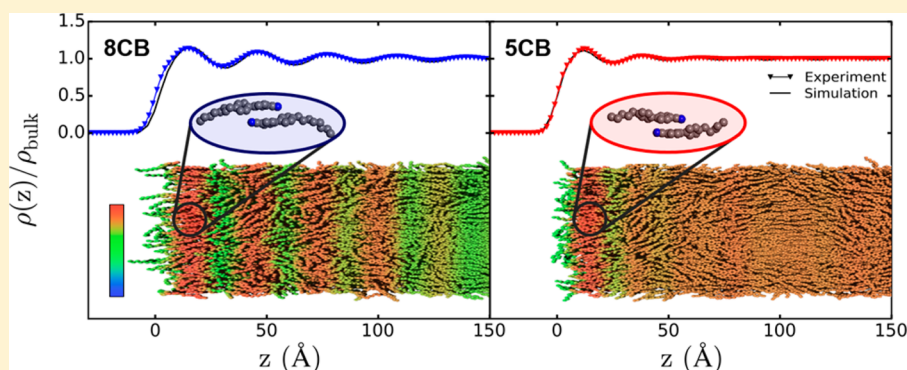
ABSTRACT: Numerous applications of liquid crystals rely on control of molecular orientation at an interface. However, little is known about the precise molecular structure of such interfaces. In this work, synchrotron X-ray reflectivity measurements, accompanied by large-scale atomistic molecular dynamics simulations, are used for the first time to reconstruct the air-liquid crystal interface of a nematic material, namely, 4-pentyl-4′-cyanobiphenyl (5CB). The results are compared to those for 4-octyl-4′-cyanobiphenyl (8CB) which, in addition to adopting isotropic and nematic states, can also form a smectic phase. Our findings indicate that the air interface imprints a highly ordered structure into the material; such a local structure then propagates well into the bulk of the liquid crystal, particularly for nematic and smectic phases.

1. INTRODUCTION

Liquid crystals (LCs) have been studied extensively, particularly in the context of display technologies and optical devices.[1−6] In the past decade, LCs have also found new applications in areas ranging from chemical separations to gas and biomolecule detection. The latter examples, which relate to the development of optical sensors, rely on orientational transitions of LC order in response to chemical cues provided by gas molecules at an LC-air interface or by biomolecules at an LC-water interface.[7−13] Regardless of the particular field of interest, it has gradually become apparent that LCs are high-fidelity reporters of interfacial events. It is therefore of considerable interest to develop a detailed understanding of LC interfaces.

The smectic and nematic states represent the two most widely used phases of thermotropic liquid crystals. In the smectic phase, LC molecules exhibit both positional and orientational order. In the nematic phase, molecules have little or no positional order but maintain considerable orientational order. In the absence of an external stimulus, the orientation of the LC molecules in the bulk depends on the nature of the

surface or the interface of the LC film. A surface may promote strong homeotropic (perpendicular) or planar alignment of the long axis of LC molecules, and the long-range order that is characteristic of LCs amplifies that alignment deep into the bulk region of the material. Lau et al. used neutron reflectivity to investigate the orientational order of 4-octyl-4′-cyanobiphenyl (8CB) smectic molecules in the vicinity of silicon substrates treated in a variety of manners.[14] They reported a surface-induced smectic layering of the molecules that was found to depend strongly on the type of surface anchoring. Pan et al. used laser-induced Freedericksz transition (LIFT) measurements of 4-pentyl-4′-cyanobiphenyl (5CB) nematic films and concluded that the essential difference between a solid homeotropic surface and an air interface is simply the faster dynamics that is observed at the air interface.[15] Some of the earliest studies of smectic liquid crystals reported that surface molecules adopt strikingly different orientations from

those observed in the bulk.[16−20] It was shown that even above the nematic-to-isotropic transition temperature, a thin layer is formed having the structure of the low-temperature (nematic) phase; that phenomenon was referred to as "surface-induced molecular ordering".[18] Pershan and Als-Nielsen pioneered the application of synchrotron X-ray reflectivity to liquid surfaces by studies of the LC-air interface, demonstrating that smectic fluctuations within a nematic phase of octyloxycyanobiphenyl (8OCB) are pinned to the interface to produce surface ordering, which propagates deeper into the bulk as the smectic transition temperature is approached.[16,21] More recently, Fukuto et al. showed that, in the presence of a few angstrom thick wetting film of fluorocarbon perfluoromethylcyclohexane (PFMC), 8CB molecules at the interface adopt homeotropic anchoring, and surface-induced smectic layering propagates into the bulk as the thickness of the wetting layer increases.[20]

This characteristic of LCs, surface-induced molecular ordering, can be used to control molecular orientation. Molecular orientation at the LC-air interface has been studied in detail for "oxycyanobiphenyl" smectic liquid crystals;[16,21−25] only a few studies, however, have focused on 8CB.[20,26] To the best of our knowledge, the molecular scale characterization of nematic LCs at the air-liquid interface has not been considered previously. This represents an important gap in the literature, especially when one considers that the vast majority of LC-interfacial adsorption (or sensing) experiments to date have been carried out with 5CB in the nematic phase. Although spectroscopic techniques, such as polarized light and fluorescence microscopy, provide a wealth of information regarding the microscopic behavior of LCs, their resolution is insufficient to extract a detailed understanding of structure in LC-air interfaces at molecular length scales.

In this work, we present a detailed examination of the molecular organization of 5CB and 8CB at the LC-air interface using advanced synchrotron X-ray reflectivity measurements and atomistic molecular dynamics simulations. Our molecular dynamics simulations and experimental characterization show that liquid crystals at free interfaces adopt a homeotropic (perpendicular) orientation with induced layer formation at the surface, even for a nematic LC such as 5CB, which does not have a bulk smectic phase.

2. MATERIALS AND METHODS

Both 4-pentyl-4′-cyanobiphenyl (5CB) and 4-octyl-4′-cyanobiphenyl (8CB) liquid crystals were purchased from Sigma-Aldrich and were used as received. Note that 5CB exhibits transitions from a crystal (Cr) to a nematic (N) state at 18 °C and is nematic at room temperature. It undergoes a transition from nematic to isotropic at 35 °C. On the other hand, at room temperature, 8CB is in the smectic A phase and undergoes a smectic-to-nematic transition at a temperature of 33.5 °C. The nematic-isotropic transition occurs at 40 °C. Samples for reflectivity measurements were prepared by spreading the liquid crystal on a 3 mm thick float glass disk (Esco Glass Co., 50 mm diameter, polished soda lime glass), which was etched with 40% hydrofluoric acid for 5 min and then treated with a surfactant (*N,N*-dimethyl-*N*-octadecyl-3-aminopropyltrimethoxysilyl chloride (DMOAP), Sigma-Aldrich). The DMOAP treatment induces normal alignment of the LC molecules at the glass surface, and hydrofluoric acid creates a fine roughness (20 nm) on the glass substrate, which improves wetting of the liquid crystal and reduces the specular reflection from the glass substrate.

Prior to film formation on the glass, the liquid crystals were heated above the nematic-isotropic (NI) temperature. Approximately 300 mg of liquid was spread over a glass disk to form a 0.2 mm thick liquid crystal film. This disk was approximately 45 mm in diameter, which

was large enough to produce a film with sufficient flatness for X-ray reflectivity measurements. The flatness of the LC interface leads to constant X-ray reflectivity as the X-ray beam is scanned across the interface at a fixed incident angle.

The glass was mounted inside a sample cell placed in a thermostat for temperature control. Incident and reflected X-ray beams passed through Mylar film windows mounted on the sides of the sample cell. The windows were sealed with Teflon-coated O-rings to provide a leak-tight cell. A Lakeshore 340 controlled the temperature of the thermostat to within ±0.01 °C.

Synchrotron X-ray experiments were performed at ChemMatCARS sector 15-ID of the Advanced Photon Source (Argonne National Laboratory) with an X-ray energy of 30 keV (X-ray wavelength λ = 0.41328 Å). To measure X-ray reflectivity at very small angles, we used a liquid surface reflectometer, which has been described in detail previously, and utilized an area detector to measure the signal and background simultaneously.[25]

As discussed in the literature, X-ray reflectivity characterizes molecular organization by probing the variation along the surface normal (z) of the electron density $\rho(z)$ averaged over the $x−y$ plane of the surface.[25] Using a monochromatic X-ray beam, reflectivity data are measured as a function of the difference between the scattered and incident wave vectors, where the wave vector transfer for specular reflection is given by $q_z = |\vec{k}_{out} - \vec{k}_{in}| = (4\pi/\lambda)\sin\alpha_i$, where $\vec{k}_{in}$ is the incident wave vector, $\vec{k}_{out}$ is the reflected wave vector, λ is the X-ray wavelength, and α_i is the angle of incidence. Background off-specular scattering was measured by shifting to either side of the specular condition by a small in-plane angle and then subtracted from the reflected intensity measured at the specular condition.[25] This signal was normalized to the incident intensity of the X-ray beam and then divided by the Fresnel reflectivity $R_F(q_z)$ prior to further analysis. The Fresnel reflectivity $R_F(q_z)$ was calculated for a theoretical LC-air interface whose electron density changes abruptly as a step-function from zero on the air side to the average value of the bulk liquid crystal (ρ_{8CB} = 0.332 e$^-$Å^{-3} and ρ_{5CB} = 0.326 e$^-$Å^{-3}). From the critical wave vector, $q_c = 4\sqrt{\pi r_e \rho_\infty}$, where r_e is the classical electron radius and ρ_∞ is the bulk electron density, the Fresnel reflectivity is given by[25]

$$R_F(q_z) = \left| \frac{q_z - \sqrt{q_z^2 - q_c^2}}{q_z + \sqrt{q_z^2 - q_c^2}} \right|^2 \tag{1}$$

For $q_z \leq q_c$, $R_F(q_z) = 1$, i.e., the X-rays are totally reflected. The critical wave vector q_c is approximately 0.0217 Å^{-1} for the 8CB-air interface and 0.0215 Å^{-1} for the 5CB-air interface. Reflectivity measurements were taken on samples whose temperatures varied over a range that encompassed the smectic-nematic transition and the isotropic transition temperatures.

Molecular dynamics simulations of 8CB and 5CB thin-films were carried out over the same temperature range as that investigated in the X-ray measurements. Free-standing films were created by exposing the lower and upper planes of a film to vacuum. A periodic simulation box of dimensions $110 \times 110 \times 400$ Å^3 was prepared with 8,000 molecules of 5CB or 8CB molecules. The united-atom model of Tibero et al.,[27] which has been shown to predict liquid-phase behavior in good agreement with experiment, was used for all calculations.

Simulations were performed in the canonical ensemble (NVT) using the Nanoscale Molecular Dynamics package (NAMD).[28] A Langevin thermostat was used to control temperature with a damping coefficient of 1 ps^{-1}. A time step of 2 fs was employed, and a spherical cutoff radius of 12 Å coupled to a smoothing function between 10 and 12 Å was also implemented. The summation of Coulomb interactions was handled using the particle mesh Ewald (PME) method with an accuracy of 10^{-6} kcal/mol. All systems were subjected to multiple intervals of 50 ns MD simulations ($6 \times 50 = 300$ ns for the 5CB films and $12 \times 50 = 600$ ns for the simulation of 8CB).[29]

3. RESULTS AND DISCUSSION

3.1. Analysis of X-ray Reflectivity Results and Calculations of Electron Density Profiles. Figure 1 shows
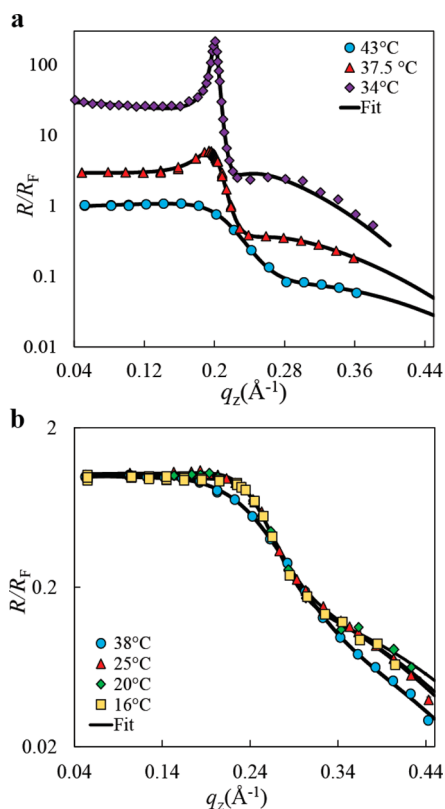
Figure 1. X-ray reflectivity measurements R/R_F from the LC-air interface for (a) 8CB and (b) 5CB. The reflectivity data are normalized to the Fresnel reflectivity, and were measured on samples whose temperatures ranged from the smectic-nematic transition to the isotropic regime of the corresponding liquid crystals ($T_{5CB\_crystal-nematic}$ = 18 °C, $T_{5CB\_nematic-isotropic}$ = 35 °C, $T_{8CB\_smectic-nematic}$ = 33.5 °C, $T_{8CB\_nematic-isotropic}$ = 40 °C). Symbols represent the experimental results, and solid dark lines depict the best fit of the empirical model to the experimental data. For 8CB, each data set has been shifted vertically for clarity.

the results of X-ray reflectivity measurements, at different temperatures, as a function of wave vector transfer q_z for 8CB and 5CB. At elevated temperature in the isotropic phase (43 °C), the experimental X-ray reflectivity data for 8CB exhibit a simple crossover around $q_z \approx 0.2$ Å^{-1} (Figure 1a). As the smectic-nematic transition temperature for 8CB is approached from above, a characteristic feature develops near this crossover, which is indicative of surface-induced smectic layering (Figure 1a). The reflectivity data have a peak at $q_z = q_0 = 0.2$ Å^{-1}, which becomes sharper as one approaches the smectic-nematic transition temperature of 8CB. The spacing of

the surface induced layers can be calculated from the peak position, which is located at $d = 2\pi/q_0 \approx 31.6$ Å for 8CB.[20]

In contrast, our reflectivity data for 5CB in the nematic phase indicate that molecular organization is almost independent of temperature. A weak peak can be observed around $q_z = q_0 = 0.24$ Å^{-1}, which corresponds to a layer spacing of $d = 2\pi/q_0 \approx 26$ Å. In the isotropic phase, 5CB does not exhibit any significant structural features.

Along the direction perpendicular to the interface, z, the average electron density over the $x-y$ plane can be calculated by fitting a "theoretical" reflectivity curve to the experimental X-ray data. In the Born approximation limit, i.e., $q_z \gg q_c$, the theoretical reflectivity can be expressed as[21,22]

$$\frac{R(q_z)}{R_F(q_z)} = \left| \frac{1}{\rho_\infty} \int \frac{\partial \langle \rho(z) \rangle}{\partial z} e^{iq_z z} \, dz \right|^2 \tag{2}$$

To describe the surface-induced layering at the vapor interface, Pershan et al.[24] proposed the following empirical expression for the total average electron density

$$\frac{\langle \rho(z) \rangle}{\rho_\infty} = \varphi_1(z) + \varphi_2(z) = \frac{1}{2}\left[1 + \mathrm{erf}\left(\frac{z}{\sqrt{2}\,\sigma} \right) \right] + \Theta(z - z_0) A e^{-(z-z_0)/\xi} \sin[2\pi(z - z_0)/d] \tag{3}$$

In eq 3, φ_1 describes the error function (erf) crossover in the electron density from the liquid crystal to the air, where σ represents the interfacial smearing due to the thermal (capillary wave) roughness of the interface. The second term, φ_2, which is temperature dependent, represents the surface-induced smectic layering that extends from the LC surface toward the bulk LC. In the latter term, $\Theta(z - z_0)$ is a step function with a value of unity for $z \geq z_0$ and zero elsewhere (where positive z extends into the LC material), A is a constant amplitude, d represents the layer spacing, and ξ is the decay length of smectic layering away from the LC-air interface. The characteristic parameters σ, z_0, A, ξ, and d in eq 3 are determined by fitting the structural model to the X-ray reflectivity data. The best fits of the model to the data are shown with lines in Figure 1, and the corresponding parameters (and temperatures) are listed in Tables 1 and 2 for 8CB and 5CB, respectively.

The average electron density profiles determined from eq 3 are shown in Figure 2. These profiles exhibit damped sinusoidal oscillations with a periodicity that corresponds to the smectic layer spacing, d. The average electron density profiles in the isotropic phase of both 8CB and 5CB consist of essentially a single smectic layer at the surface of the LC. The density decays rapidly to the bulk value beyond that layer. There are, however, pronounced differences between 8CB and 5CB in the nematic phase. Although density fluctuations at the 8CB-vapor interface are strongly temperature dependent, they exhibit only a weak temperature dependence for 5CB. Even at 16 °C, where 5CB should be in its crystalline phase, there are no considerable

Table 1. Layer Parameters Obtained from the Best Fit of the Empirical Model (eq 3) to the Experimental Reflectivity Data from the 8CB-Air Interface

T (°C)	d (Å)	ξ (Å)	A	σ (Å)	z_0 (Å)
34	31.19 ± 0.02	280 ± 10	0.09 ± 0.005	4.6 ± 0.3	5.7 ± 0.3
37.5	31.24 ± 0.05	65 ± 2	0.153 ± 0.006	4.1 ± 0.2	7.1 ± 0.2
43	29.7 ± 0.4	18.4 ± 1.5	0.29 ± 0.03	3.6 ± 0.2	9.3 ± 0.3

Table 2. Layer Parameters Obtained from the Best Fit of the Empirical Model (eq 3) to the Experimental Reflectivity Data from the 5CB-Air Interface

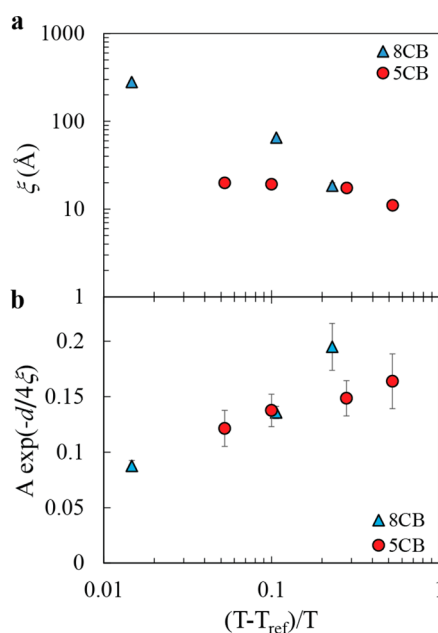| T (°C)	d (Å)	ξ (Å)	A	σ (Å)	z_0 (Å)
16	25.3 ± 0.3	21.7 ± 1.4	0.15 ± 0.02	3.33 ± 0.07	6.6 ± 0.3
20	25.5 ± 0.3	19.1 ± 1.3	0.19 ± 0.02	3.2 ± 0.1	7.1 ± 0.2
25	26.3 ± 0.3	17.4 ± 1.4	0.22 ± 0.02	3.3 ± 0.1	7.3 ± 0.3
38	25.5 ± 0.4	11.0 ± 0.8	0.3 ± 0.04	3.05 ± 0.17	8.1 ± 0.3
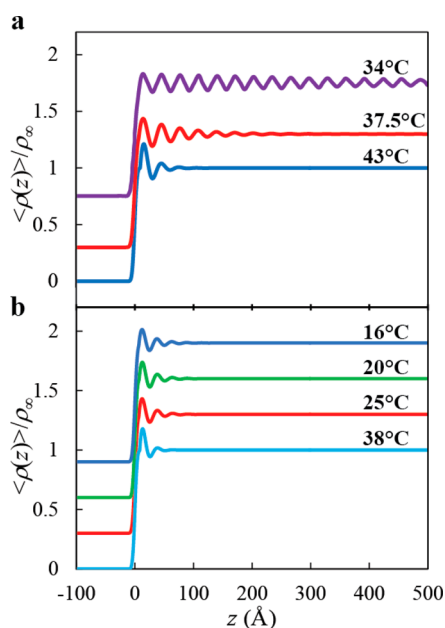
Figure 2. Average electron density along the z direction (normal) from the air-liquid crystal interface calculated using eq 3 and the best fit of the model to the X-ray reflectivity data. Results are shown for (a) 8CB and (b) 5CB. The X-ray reflectivity measurements and subsequent average electron density calculations were performed for a temperature range that includes the smectic-nematic transition and the isotropic regime of the corresponding materials. All curves, except for those at 38 and 43 °C, were offset for visual clarity.


Figure 3. (a) Correlation length and (b) oscillation amplitude at the center of the first smectic layer as a function of reduced temperature $(T - T_{ref})/T$ for the 8CB-air and 5CB-air interfaces. Here, T_{ref} is the reference temperature at which 8CB and 5CB undergo smectic-nematic transition (33.5 °C) and crystalline-nematic transition (18 °C), respectively. The 5CB data are reported at $T = 19, 20, 25,$ and 38 °C. The X-ray reflectivity measurements and average electron density of 5CB at $T = 19$ °C are presented in Figure S3, and the corresponding layer parameters are listed in Table S1.

differences and the observed electron density profile does not vary much.

As we approach the smectic-nematic transition temperature of 8CB ($T = 33.5$ °C), the average electron density for 8CB exhibits pronounced sinusoidal oscillations of constant amplitude that penetrate far into the bulk region along the z direction. The length scale over which the surface-induced smectic layers persist is given by a temperature-dependent correlation length ξ, which is plotted in Figure 3a. The period of the oscillations corresponds to the induced-smectic layer spacing, which is approximately 31 Å for 8CB and 26 Å for 5CB.[14,19,20,29] Considering that the molecules have an alkyl tail whose effective length is approximately 10.5 Å for 8CB and 6.5 Å for 5CB, and that a cyanobiphenyl core has a length of approximately 12 Å,[30] one could infer that each layer should consist of overlapping molecules arranged in a bilayer structure that is approximately 1.6 times larger than the length of an individual molecule. To elucidate the molecular origins of such layer spacing values, we turn in the next section to atomistic molecular dynamics simulations of free-standing films of 5CB and 8CB over the same temperature range as that considered in the experiments.

Figure 3a shows the correlation length ξ of 8CB and 5CB as a function of reduced temperature $(T - T_{ref})/T$ on a log–log

scale. T_{ref} is the reference temperature at which 8CB and 5CB undergo smectic-nematic transition (33.5 °C) and crystalline-nematic transition (18 °C), respectively. Compared to 5CB, the 8CB-air interface induces a smectic layering that has a much longer penetration depth (Figure 3a).

We further investigated the effect of the air interface on the organization of 5CB and 8CB molecules by calculating the amplitudes of the normalized average electron density at the maximum of the first peak using $A\exp(-d/4\xi)$ (Figure 3b), which is located approximately at $z = d/2$. The amplitude increases with temperature, and it reaches its highest value when both 8CB and 5CB are in their isotropic phase (Figure 3b). The maxima in the average electron density correspond to the cyanobiphenyl head groups, and the minima correspond to the regions where the alkyl tails and the CH_3 groups are located. Although X-ray reflectivity data reveal essential information about the layering structure of the liquid crystals, some central questions regarding the molecular arrangement of the mesogens within the layers still remain. In the following sections, atomistic molecular dynamics simulations are used to provide atomic-level information about the specific organization of the liquid crystal molecules within the free-standing films.
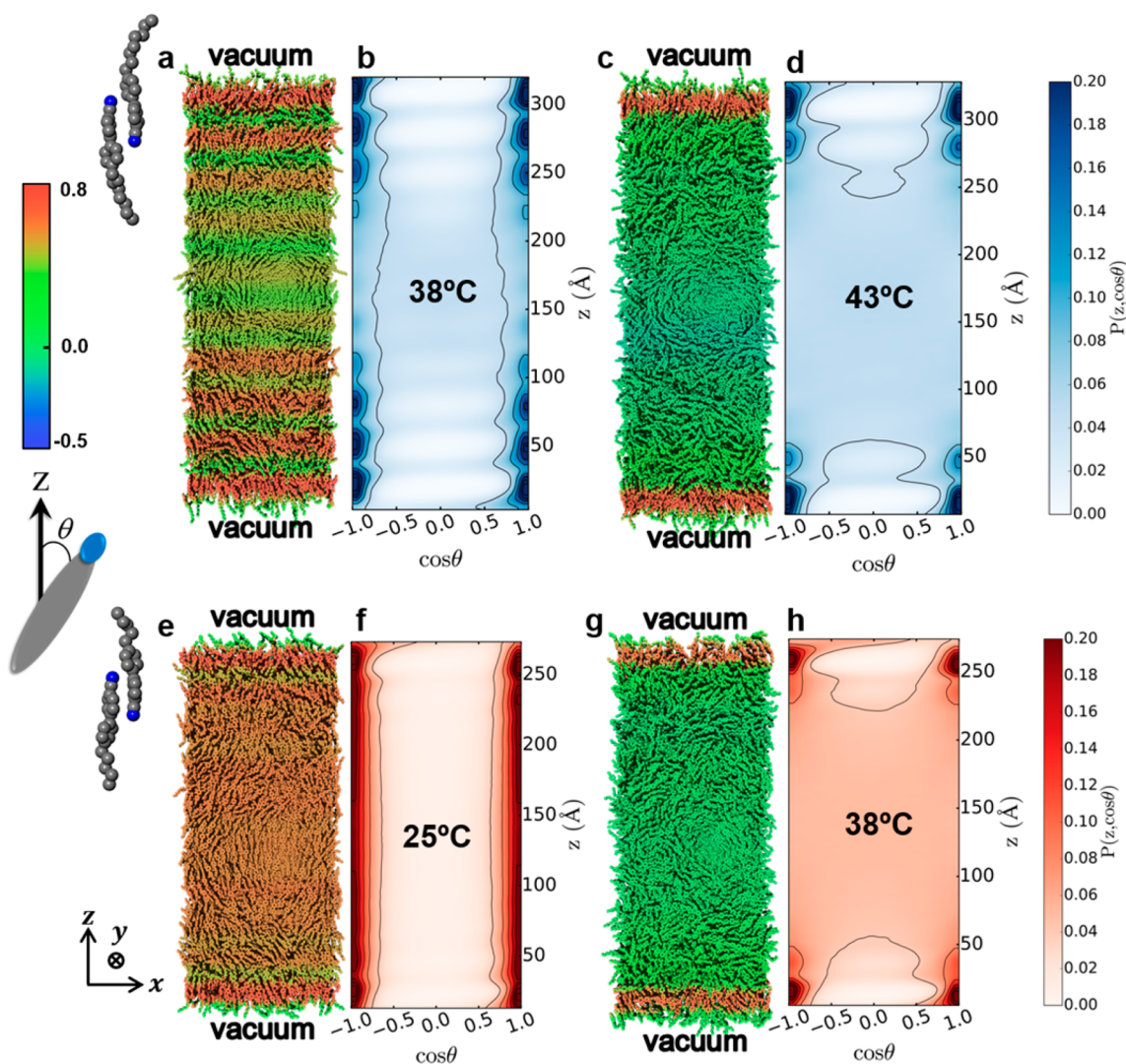
Figure 4. Ensemble average of the second Legendre polynomial P_2 and the two-dimensional histograms of orientational probabilities $P(z, \cos \theta)$ of 8CB and 5CB thin films exposed to vacuum on the lower and upper planes according to molecular dynamics simulations: (a,b) 8CB in nematic phase at 38 °C, (c,d) 8CB in isotropic phase at 43 °C, (e,f) 5CB in nematic phase at 25 °C, and (g,h) 5CB in isotropic phase at 38 °C. Panels a, c, e, and g illustrate simulation snapshots with ensemble averaged P_2 overlaid in color according to the color scheme in the upper left. Panels b, d, f, and h show the orientational probabilities $P(z, \cos \theta)$ according to the color schemes on the right. Molecules adopt an antiparallel orientation within the first layer near the surface regardless of the temperature (within the examined temperature range in this study) or the type of mesogen. The induced oscillatory surface layering extends far away from the surface in the nematic phase of 8CB and exhibits connecting interlayer regions of lower order. The isotropic profiles of 5CB and 8CB are nearly identical, showing a characteristic well-ordered layer at the surface and random distributions of the molecules throughout the subsurface regions.

3.2. Molecular Dynamics Simulations of Free-Standing Films of 8CB and 5CB. The specular X-ray reflectivity experiments offer only one-dimensional information along the direction normal to the film surface. It is therefore insightful to perform atomistic molecular dynamics simulations of the same systems using validated force fields, which enable one to infer three-dimensional structural and dynamical information.

3.2.1. Molecular Organization and Orientational Probabilities. We begin by quantifying the average orientation of 8CB and 5CB molecules with respect to a predefined axis along the surface normal, i.e., $\hat{z} = (0,0,1)$, by computing the second Legendre polynomial $P_2(z)$ according to

$$\langle P_2(z) \rangle = \left\langle \frac{3}{2}\cos^2 \theta - \frac{1}{2} \right\rangle \tag{4}$$

In this equation, θ defines the angle between the long molecular axis of the mesogens and the $\hat{z}$ axis (Figure 4), and $\langle ... \rangle$ denotes the ensemble average. In addition to $P_2(z)$, one can generate two-dimensional (2D) maps of molecular orientation probabilities at any given distance from the surface $P(z, \cos \theta)$ (Figure 4b,d,f,h). The corresponding 2D plots allow one to qualitatively assess the preferred orientation of the molecular dipoles within a smectic bilayer of the thin films. Molecules may align along a specific axis ($\hat{z}$ axis for instance), but their dipoles may point in the positive or negative directions. Such directional specificity often has significant structural and dynamical consequences.

Three to four interface-induced layers are clearly present near the 8CB-vacuum interface at 38 °C; they appear as red-green stripes in the color-coded profile of P_2. These induced layers gradually fade out as one moves away from the 8CB-vacuum

interface. The formation of the low order regions within the smectic layers (the green bands between the red bands in Figure 4a) is a characteristic signature of smectic-forming mesogens with significant molecular flexibility, such as 8CB.[31] We mention in passing that the molecular flexibility of 8CB offers a mechanism for layer-to-layer permeation of the molecules.[31−33] This mechanism involves (i) a straight pathway with minimal reorientation of the 8CB molecules and (ii) a "parking lot" mechanism with significant reorientation of the molecules. The specific details of such translational diffusion mechanisms will be the subject of a future investigation. The 2D map of molecular orientations shows that the smectic layers near the surface consist of tightly packed molecules having an antiparallel orientation of molecular dipoles (Figure 4b).[34] The 8CB molecules are evidently unable to assume a strict antiparallel orientation in the central regions of the thin film, where a quasi-uniform distribution of molecular orientation is observed (Figure 4b).

In the isotropic phase of 8CB at 43 °C, strong anchoring induces a highly ordered layer near the surface, followed by a secondary sublayer that exhibits a smaller degree of molecular order (Figure 4c, d).

In the nematic phase of 5CB, the molecules are oriented preferentially along the surface normal as evident by the high value of P_2 throughout the film (Figure 4e and Figure S1). The two quasi-symmetric narrow bands in the 2D histograms of the molecular orientation maps (Figure 4f) indicate that (i) 5CB molecules adopt an antiparallel orientation throughout the film, including the surface and bulk regions, and (ii) the low order regions within the smectic-like layers are less clearly defined in contrast to the nematic phase of 8CB. As such, one could anticipate that molecular transport mechanisms in free-standing films of nematic 5CB are different from those of true smectic A phases. The one-dimensional profile of P_2 and 2D histograms of molecular orientations in the isotropic phase of 5CB (Figure 4g,h) are similar to those observed in the isotropic phase of 8CB at 43 °C, where a single surface layer is formed and the molecules do not assume a preferred orientation beyond that imposed at the interface by the homeotropic anchoring.

3.2.2. Electron Density Profiles and Correlations with Reflectivity Measurements. The configurations generated from simulations were also used to compute the electron density profiles of 8CB and 5CB thin films in the nematic and isotropic phases. The results are compared to those of our experimental measurements in Figure 5. We note here that the experimental electron density profiles were obtained by fitting a structural model to reflectivity data (see section 3.1). One could also obtain the electron density profiles from atomistic simulations and then compute the Fourier transform of the derivative of the electron density to arrive at simulated reflectivity profiles (see eq 2). In our work, we chose to compare the real space electron density profiles because unlike the micrometer-thick films employed in experiments, where the liquid crystal remains in contact with air on the upper plane of the film and is anchored to a DMOAP-coated glass substrate on the lower plane, the simulated ~30 nm thick free-standing films are in contact with vacuum (i.e., air) on both sides. As such, the reflectivity signals may pick up some surface information (from the second half of the thin film). We also emphasize that the structural model used in this work is able to reproduce the profile of our reflectivity data with considerable precision (Figure 1).[20,24]

To compute electron density profiles near the free surfaces of 8CB and 5CB, the simulation box is binned along the surface
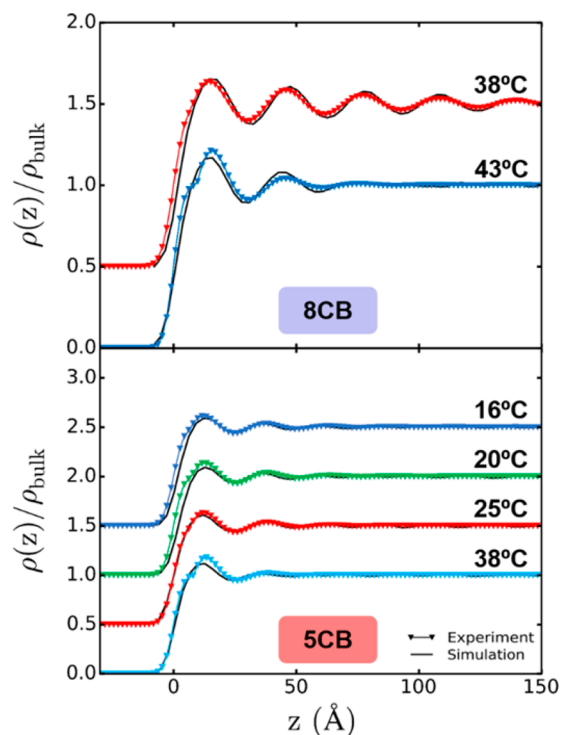

Figure 5. Comparison of the simulated electron density profiles (continuous lines) with the profiles obtained from the X-ray reflectivity measurements (symbols connected by lines). The electron density profiles from the molecular dynamics simulations reproduce the main features of the experimental profiles, including the amplitude of the first peak, propagation length, and oscillation period.

normal. The proper number of electrons (considering partial charges of atoms) is then placed at the positions of the atomic nuclei.[35] The electron density profiles generated in this manner are in quantitative agreement with the experimental data.

The main features of the electron density profiles here include (i) the amplitude of the first peak near the free surface, (ii) the oscillation/propagation length, and (iii) the oscillation period. The simulated electron density profiles of 8CB and 5CB reproduce these essential structural features very well. The minor deviations from the X-ray profiles, particularly in the isotropic phases of 5CB at 38 °C and 8CB at 43 °C, could be ascribed to the accuracy of the force field, which reproduces the nematic-isotropic transition temperatures of 8CB and 5CB with a ±4 K deviation from the experimental values. Alternatively, the detailed structure in the experimental profiles near $z = 0$ that is not reproduced in the simulations may be an artifact of the model used to fit the reflectivity data, which is not revealed by fits to the data measured over the experimentally accessible range of q_z.

3.2.3. Scalar Order Parameter and Components of Director. We also evaluated the extent of molecular ordering and the preferred molecular alignment throughout the entire free-standing films by computing profiles of the scalar order parameter S and director $\boldsymbol{n}$ using the ensemble average of the tensorial orientation order parameter $\mathbf{Q}$[36]

$$\mathbf{Q} = \frac{3}{2}\left\langle \mathbf{aa} - \frac{1}{3}\mathbf{I} \right\rangle \qquad (5)$$
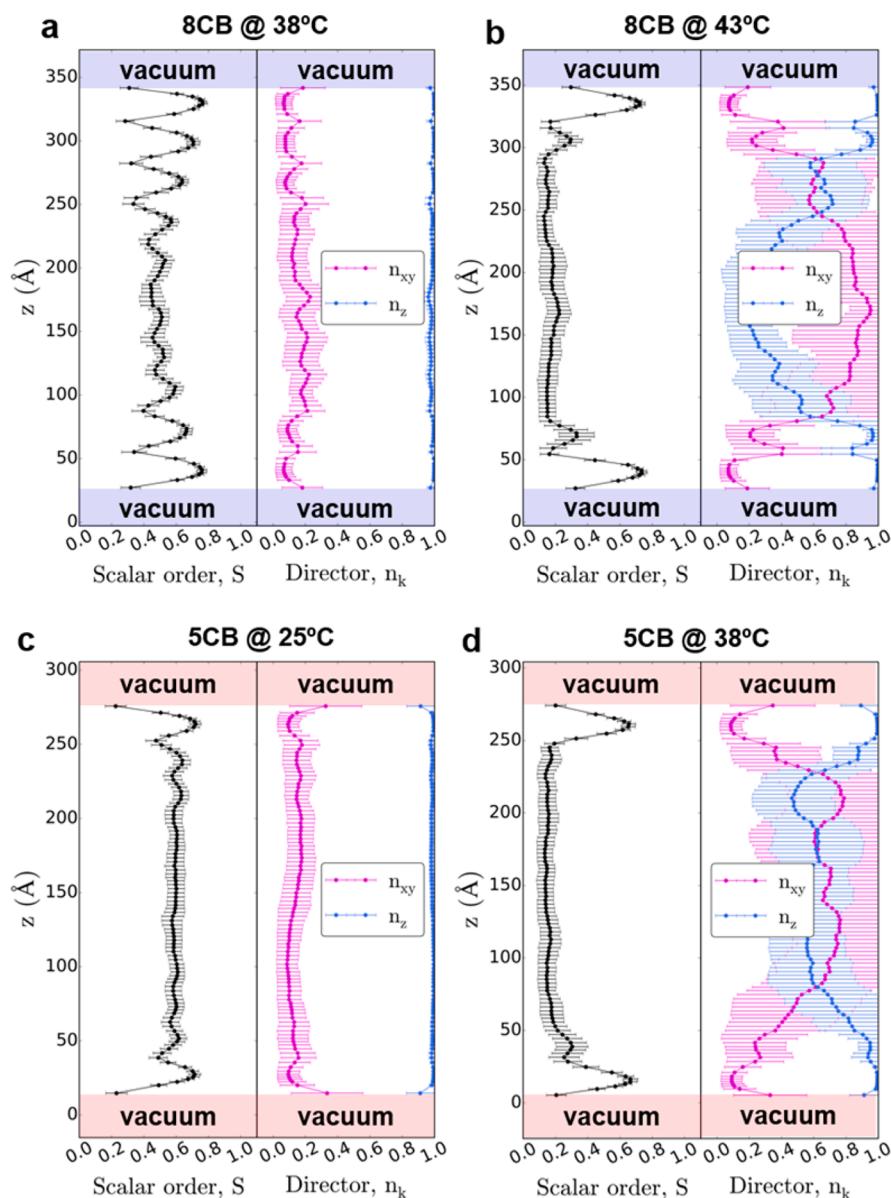
Figure 6. Orientational features (scalar order parameter S and components of director n) of free-standing thin-films of 5CB and 8CB obtained from atomistic molecular dynamics simulations. These profiles were obtained by construction and diagonalization of the Q tensor for (a) 8CB in nematic phase at 38 °C, (b) 8CB in isotropic phase at 43 °C, (c) 5CB in nematic phase at 25 °C, and (d) 5CB in isotropic phase at 38 °C. In the nematic phase of 8CB, the formation of several surface-induced layers is visible in the sinusoidal oscillations of S. In the nematic phase of 5CB, two induced surface layers are formed with sinusoidal fluctuation and homeotropic anchoring. The perpendicular orientation near the free surface spreads over the entire thin film. Here, n_z is the z component of the director and $n_{xy} = \sqrt{(n_x^2 + n_y^2)}$. The error bars show the standard deviation of the computed values over the final 30 ns block of MD simulations.

In this equation, Q is a traceless and symmetric tensor, I is the identity matrix, a is the long molecular axis of the 5CB and 8CB molecules, and $aa = \vec{a}\vec{a}^T$ represents the dyadic product.

Figure 6 shows representative order parameter and director profiles for 8CB in the nematic and isotropic phases. In the nematic phase of 8CB at 38 °C, the profile of the scalar order parameter S is similar to that of P_2 (Figure 4a and 6a). Oscillations in S indicate the formation of several surface-induced layers in the nematic phase of 8CB. The molecules, on average, are oriented along the surface normal. In the isotropic phase, the scalar order parameter shows that a distinct smectic-like layer is formed near the interface (Figure 6b).

The oscillations in S in the nematic phase of 8CB reach the bulk from both sides of the film. The corresponding correlation length is in fact larger than half of the film thickness. As such, an inner layer with an average S of ∼0.4 is formed near the center because our film thickness (which is determined by the number of 8CB molecules in the simulation) is not necessarily an integer product of the smectic layer-spacing d (Figure 6 and Table 1). The components of the nematic director show that the molecules are preferentially oriented perpendicular to the surface, as revealed by the large values of n_z, which remain near unity throughout the film (Figure 6a).

In the isotropic phase of 8CB at 43 °C, a sharp peak of the scalar order parameter can be seen near the free surface (Figure
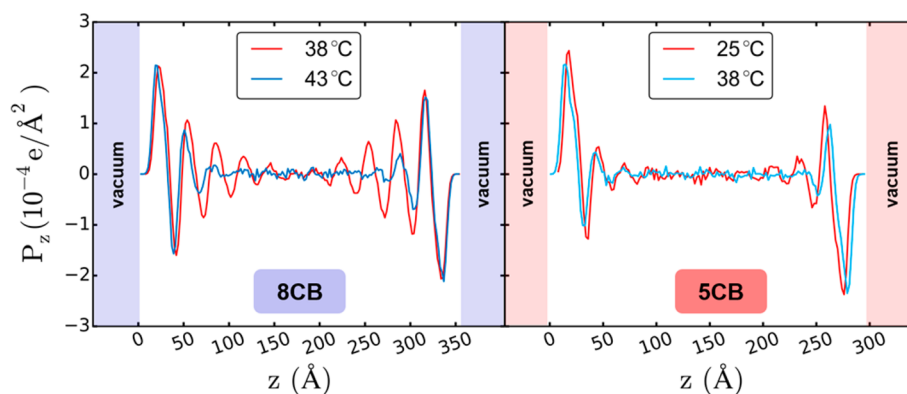
Figure 7. Average polarization density profiles for free-standing films of 8CB (left) and 5CB (right) in the nematic and isotropic regimes. Surface molecules orient their polar heads toward the bulk regions of the films, thereby minimizing the surface free energy. Subsurface molecules point their dipoles in opposite directions to those of the surface molecules in order to form antiparallel configurations.

6b). Such a distinct peak of S ($S = 0.75$) near the vacuum region indicates that surface molecules remain highly ordered even in the isotropic regime at 43 °C. Following that distinctive primary peak, one can observe an additional secondary peak, which reaches a value of 0.4 at the maximum. In the areas beyond these surface-induced layers, which are approximately 60 Å thick, the average value of S remains close to 0.1, which is a typical value for isotropic LC phases (Figure 6b). The profiles of the components of the director also show that induced smectic-like layers are formed near the surface and that the film becomes truly isotropic beyond a 60 Å distance from the free surface. The highly ordered smectic-like layers in the nematic and isotropic phases of 8CB suggest that the entropic loss in those regions is compensated by enthalpic gains arising from the dense packing of the 8CB molecules.

Our simulations of 5CB in the nematic phase (at 20 and 25 °C) show that two smectic-like surface layers are formed (Figure 6c and Figure S2). Below the crystal-nematic transition temperature (16 °C), the film shows slightly higher order near the surface (Figure S2). The penetration length of these surface-induced layers is less than 100 Å with an average oscillation period of ~25 Å, which is in excellent agreement with the experimental data (Table 2).[19,37] These moderate oscillations of the scalar order profile are different from those observed in the nematic phase of 8CB (see Figure 6a). The orientation of the molecules in the central region of the film is bulk-like, but the homeotropic surface anchoring determines the preferred alignment direction of the nematic field across the entire film (Figure 6c and Figure S2). In the isotropic phase of 5CB at 38 °C, strong homeotropic anchoring remains in effect, and the scalar order parameter exceeds 0.6 near the surface. The 5CB molecules near the interface form a single dimer layer with 25 Å thickness. The orientational order of the molecules decays rapidly in the regions beyond this surface layer (Figure 6d).

3.2.4. Polarization Density Profiles. The electron density profiles provide useful information about molecular organization at interfaces but contain little or no quantitative information concerning the preferred orientation of the molecular dipoles. The profiles of the average polarization density, on the other hand, offer such information. Here, we calculate the average polarization density of liquid crystal molecules along the surface normal using a well-established method.[29,38] The local polarization density at position r in a system comprising point dipoles μ_i located at positions i is the summation of dipoles at that position

$$\mathbf{P}(\mathbf{r}) = \sum_i \boldsymbol{\mu}_i \delta(\mathbf{r} - \mathbf{r}_i)$$

(6)

where $P(r)$ is the local average polarization density and $\delta(r)$ is the Dirac delta function. For a single component system in a zero electric field environment, one expects to realize a zero-sum profile of polarization density. The profiles of the average polarization density of 8CB and 5CB films show an oscillatory feature near the free surface that extends far into the films. The nonzero profiles of polarization density near the surface imply that subsurface molecules are unable to fully cancel out the oriented dipoles of the first molecular layer due to a sharp dielectric discontinuity between the vacuum and the LC. This finite polarization density in the vicinity of the LC-vacuum interface generates an electric field inside the LC film, which disturbs the net orientation of the molecular dipoles of the second molecular layer and eventually generates an alternating net orientation of the molecular dipoles in positive and negative directions (Figure 7). The positive value of the first peak near the lower plane of the films indicates that the polar cyano head groups points toward the bulk region (to avoid the vacuum). The profile of polarization densities possesses a point symmetry around the center of the films because the molecular dipoles in the lower and upper half of the films are oriented in opposite directions, to eventually produce a zero-sum profile. As expected, 8CB in the nematic phase shows the familiar characteristic smectic layering that was also observed in the scalar order parameter and electron density profiles. The average polarization density through the bulk regions of the 5CB film and the isotropic phase of 8CB remains close to zero, showing that the molecular dipoles cancel each other out in those regions.

4. CONCLUSIONS

A combination of synchrotron X-ray reflectivity measurements and molecular dynamics simulations was used to arrive at a detailed picture of interfacial molecular organization in two of the most widely used nematic (5CB) and smectic (8CB) liquid crystals. The agreement between experiment and simulation is quantitative and has revealed a number of previously unknown features. Our results show that, at the air interface, both 5CB and 8CB adopt a homeotropic orientation and exhibit well-defined surface-induced layers at the surface. The nematic

system 5CB shows two surface-induced smectic layers at the 5CB-air interface. The smectic forming material 8CB induces multiple distinct surface-induced smectic layers whose penetration depth is much longer. In the isotropic phase of both 5CB and 8CB, however, only a single dominant layer is formed.

We are currently extending the X-ray reflectivity measurements to the study of the LC-aqueous electrolyte interfaces to understand the effects of electrostatic interactions and external stimuli on the interfacial anchoring energy and LC orientational ordering. These results will be particularly important in guiding the design of responsive LC interfaces for sensing chemicals and biological molecules.

ASSOCIATED CONTENT

ⓢ Supporting Information

The Supporting Information is available free of charge on the ACS Publications website at DOI: 10.1021/jacs.7b00167.

> Molecular organization and orientational probabilities of 5CB free-standing films at 16 and 20 °C, and X-ray reflectivity measurements at 19 °C (PDF)

AUTHOR INFORMATION

Corresponding Authors
*roux@uchicago.edu (B.R.)
*schloss@uic.edu (M.L.S.)
*depablo@uchicago.edu (J.J.d.P.)

ORCID ⃝
Binhua Lin: 0000-0001-5932-4905
Juan J. de Pablo: 0000-0002-3526-516X

Author Contributions
¶M.S. and H.R. contributed equally to this work.

Notes
The authors declare no competing financial interest.

ACKNOWLEDGMENTS

REFERENCES

(1) Assouline, G.; Hareng, M.; Leiba, E. *Electron. Lett.* **1971**, *7* (23), 699−700.
(2) Cheng, H.-C.; Yan, J.; Ishinabe, T.; Sugiura, N.; Liu, C.-Y.; Huang, T.-H.; Tsai, C.-Y.; Lin, C.-H.; Wu, S.-T. *J. Disp. Technol.* **2012**, *8* (2), 98−103.
(3) Klein, S. *Liq. Cryst. Rev.* **2013**, *1* (1), 52−64.
(4) Peng, F.; Gou, F.; Chen, H.; Huang, Y.; Wu, S.-T. *J. Soc. Inf. Disp.* **2016**, *24* (4), 241−245.
(5) Yaniv, Z. *Photonics Spectra* **1989**, *23* (4), 95−97.
(6) Takane, Y.; Kawasumi, Y.; Sato, M.; Horie, T.; Ishibashi, T. *Breast Cancer* **2016**, *23* (4), 561−567.
(7) Bukusoglu, E.; Wang, X. G.; Martinez-Gonzalez, J. A.; de Pablo, J. J.; Abbott, N. L. *Adv. Mater.* **2015**, *27* (43), 6892−6898.
(8) Carlton, R. J.; Hunter, J. T.; Miller, D. S.; Abbasi, R.; Mushenheim, P. C.; Tan, L. N.; Abbott, N. L. *Liq. Cryst. Rev.* **2013**, *1* (1), 29−51.
(9) Carlton, R. J.; Ma, C. D.; Gupta, J. K.; Abbott, N. L. *Langmuir* **2012**, *28* (35), 12796−12805.
(10) Lin, I. H.; Miller, D. S.; Bertics, P. J.; Murphy, C. J.; de Pablo, J. J.; Abbott, N. L. *Science* **2011**, *332* (6035), 1297−1300.
(11) Moreno-Razo, J. A.; Sambriski, E. J.; Abbott, N. L.; Hernandez-Ortiz, J. P.; de Pablo, J. J. *Nature* **2012**, *485* (7396), 86−89.
(12) Sadati, M.; Apik, A. I.; Armas-Perez, J. C.; Martinez-Gonzalez, J.; Hernandez-Ortiz, J. P.; Abbott, N. L.; de Pablo, J. J. *Adv. Funct. Mater.* **2015**, *25* (38), 6050−6060.
(13) Sen, A.; Kupcho, K. A.; Grinwald, B. A.; VanTreeck, H. J.; Acharya, B. R. *Sens. Actuators, B* **2013**, *178*, 222−227.
(14) Lau, Y. G. J.; Richardson, R. M.; Cubitt, R. *J. Chem. Phys.* **2006**, *124* (23), 234910.
(15) Pan, R. P.; Hsiung, H.; Shen, Y. R. *Phys. Rev. A: At., Mol., Opt. Phys.* **1987**, *36* (11), 5505−5508.
(16) Als-Nielsen, J.; Christensen, F.; Pershan, P. S. *Phys. Rev. Lett.* **1982**, *48* (16), 1107−1110.
(17) delRio, E. M.; deMiguel, E. *Phys. Rev. E: Stat. Phys., Plasmas, Fluids, Relat. Interdiscip. Top.* **1997**, *55* (3), 2916−2924.
(18) Martinez-Miranda, L. J.; Hu, Y. *J. Appl. Phys.* **2006**, *99* (11), 113522.
(19) Roscioni, O. M.; Muccioli, L.; Della Valle, R. G.; Pizzirusso, A.; Ricci, M.; Zannoni, C. *Langmuir* **2013**, *29* (28), 8950−8958.
(20) Fukuto, M.; Gang, O.; Alvine, K. J.; Ocko, B. M.; Pershan, P. S. *Phys. Rev. E* **2008**, *77* (3), 031607.
(21) Pershan, P. S.; Als-Nielsen, J. *Phys. Rev. Lett.* **1984**, *52* (9), 759−762.
(22) Ocko, B. M.; Braslau, A.; Pershan, P. S.; Als-Nielsen, J.; Deutsch, M. *Phys. Rev. Lett.* **1986**, *57* (1), 94−97.
(23) Pershan, P. S. *J. Phys. Chem. B* **2009**, *113* (12), 3639−3646.
(24) Pershan, P. S.; Braslau, A.; Weiss, A. H.; Als-Nielsen, J. *Phys. Rev. A: At., Mol., Opt. Phys.* **1987**, *35* (11), 4800−4813.
(25) Pershan, P. S.; Schlossman, M. L.; Pershan, P. S.; Schlossman, M. L. *Liquid Surfaces and Interfaces: Synchrotron X-Ray Methods* **2012**, 88−172.
(26) Palermo, M. F.; Muccioli, L.; Zannoni, C. *Phys. Chem. Chem. Phys.* **2015**, *17* (39), 26149−26159.
(27) Tiberio, G.; Muccioli, L.; Berardi, R.; Zannoni, C. *ChemPhysChem* **2009**, *10* (1), 125−136.
(28) Phillips, J. C.; Braun, R.; Wang, W.; Gumbart, J.; Tajkhorshid, E.; Villa, E.; Chipot, C.; Skeel, R. D.; Kale, L.; Schulten, K. *J. Comput. Chem.* **2005**, *26* (16), 1781−1802.
(29) Ramezani-Dakhel, H.; Sadati, M.; Rahimi, M.; Ramirez-Hernandez, A.; Roux, B.; de Pablo, J. J. *J. Chem. Theory Comput.* **2017**, *13*, 237−244.
(30) Leadbetter, A. J.; Durrant, J. L. A.; Rugman, M. *Mol. Cryst. Liq. Cryst.* **1977**, *34* (10), 231−235.
(31) Mukherjee, B.; Peter, C.; Kremer, K. *Phys. Rev. E* **2013**, *88* (1), 010502.

(32) Guégan, R.; Morineau, D.; Lefort, R.; Moréac, A.; Béziel, W.; Guendouz, M.; Zanotti, J. M.; Frick, B. *J. Chem. Phys.* **2007**, *126* (6), 064902.

(33) Lefort, R.; Morineau, D.; Guegan, R.; Ecolivet, C.; Guendouz, M.; Zanotti, J. M.; Frick, B. *Phys. Chem. Chem. Phys.* **2008**, *10* (20), 2993−2999.

(34) Guyotsionnest, P.; Hsiung, H.; Shen, Y. R. *Phys. Rev. Lett.* **1986**, *57* (23), 2963−2966.

(35) Giorgino, T. *Comput. Phys. Commun.* **2014**, *185* (1), 317−322.

(36) Kléman, M.; Lavrentovich, O. D. *Soft Matter Physics: An Introduction (Partially Ordered Systems)*; Springer: New York, 2003.

(37) Ruths, M.; Zappone, B. *Langmuir* **2012**, *28* (22), 8371−8383.

(38) Stern, H. A.; Feller, S. E. *J. Chem. Phys.* **2003**, *118* (7), 3401−3412.